Continuously Improved Photocatalytic Performance of Zn₂SnO₄/SnO₂/Cu₂O Composites by Structural Modulation and Band Alignment Modification

Tiekun Jia [1,*] **, Junchao An** [1,*] **, Dongsheng Yu** [1] **, Jili Li** [1] **, Fang Fu** [1] **, Kun Wang** [1] **and Weimin Wang** [2]

[1] School of Materials Science and Engineering, Luoyang Institute of Science and Technology, Wangcheng Road 90#, Luoyang 471023, China; dongsh_yu@163.com (D.Y.); lijili328@126.com (J.L.); fufang1@126.com (F.F.); wk13007581560@163.com (K.W.)

[2] State Key Lab of Materials Synthesis and Processing, Wuhan University of Technology, Wuhan 430070, China; wangwm@hotmail.com

* Correspondence: tiekunjia@126.com or tkjia@whut.edu.cn (T.J.); superjun@tju.edu.cn (J.A.); Tel./Fax: +86-379-65928196 (T.J.)

✓ check for updates

Abstract: Improving the photocatalytic performance of multi-component photocatalysts through structural modulation and band alignment engineering has attracted great interest in the context of solar energy utilization and conversion. In our work, Zn₂SnO₄/SnO₂ hierarchical architectures comprising nanorod building block assemblies were first achieved via a facile solvothermal synthesis route with lysine and ethylenediamine (EDA) as directing agents, and then chemically etched in NaOH solution to enlarge the surface area and augment active sites. The etched Zn₂SnO₄/SnO₂ hierarchical architectures were further decorated by Cu₂O nanoparticles though an in situ chemical deposition method based on band alignment engineering. In comparison with unetched Zn₂SnO₄/SnO₂, the specific surface area of Zn₂SnO₄/SnO₂/Cu₂O hierarchical architectures became larger, and the responsive region and absorbance intensity became wider and higher in the whole visible-light range. Zn₂SnO₄/SnO₂/Cu₂O hybrid photocatalysts presented enormously improved visible-light photocatalytic behaviour for Rhodamine B (RhB) decomposition. The enhancement of photocatalytic behaviour was dominantly attributed to the synergy effect of the larger specific surface area, higher light absorption capacity, and more effective photo-induced charge carrier separation and migration. A proposed mechanism for the enormously promoted photocatalytic behaviour is brought forth on the basis of the energy-band structure combined with experimental results.

Keywords: Zn₂SnO₄/SnO₂; Cu₂O decoration; structural modulation; band alignment; photodegradation mechanism

1. Introduction

As one of the widely investigated ternary oxide materials in the application of photodegrading pollutants [1–6], Zn₂SnO₄ (ZSO) has the prominent advantages of relatively high electron mobility and long-term chemical stability. However, limited to its wide bandgap and unfavorable recombination rate, the photocatalytic efficiency of pure ZSO is not satisfied. Thus, researchers have taken some approaches, for instance, ion doping [2], morphological modulation [3–6], and coupling composites [7–16], to improve the photocatalytic behavior of ZSO based photocatalyst. Among those strategies mentioned above, relevant reports on doping in ZSO are very limited, probably because the concentration of dopants is not easily controlled and the impurity level can act not only as a platform for electron transition, but also serve as a recombination center. Further, we all know that it is very difficult for a single component photocatalyst to overcome the intrinsic drawbacks of a low quantum rate and

high recombination rate only by morphological modulation. In this regard, constructing composites is one of the most facile and efficient solutions, because the construction of coupling ZSO with other matchable photocatalysts is beneficial for prolonging the lifespan of photo-generated charge carriers and accelerating charge carrier separation [14–17].

As previously reported [7–9,13–15], SnO_2 is available to construct ZSO/SnO_2 composites displaying the improvement of photodegradation rate. For instance, Chen et al. [7] took a one-pot hydrothermal synthesis method to fabricate SnO_x/Zn_2SnO_4 composites, which exhibited a higher and more stable photocatalytic performance toward the degradation of MO and gaseous C_6H_6 under UV light irradiation. Junploy et al. [8] reported an approach involving co-precipitation combined with calcination for the synthesis of Zn_2SnO_4/SnO_2, and the results showed that the as-obtained Zn_2SnO_4/SnO_2 displayed improved photocatalytic efficiency toward the degradation of MB under UV light illumination, as compared to Zn_2SnO_4 and SnO_2. Most previously reported studies were focused on the improvement of UV-light photocatalytic behavior over Zn_2SnO_4/SnO_2 photocatalysts, while the relevant studies on visible light photocatalytic activity were relatively scarce, probably because both Zn_2SnO_4 and SnO_2 belong to the group of wide band-gap photocatalysts. Generally, the photocatalytic performance in visible-light region over Zn_2SnO_4/SnO_2 coupling composites is conceivably triggered by defect states originating from oxygen vacancy or interstitial ions. Han et al. [13] fabricated double-shell Zn_2SnO_4/SnO_2 microboxes with superior photocatalytic performance under sun-light illumination. Zhang et al. [14] designed a reduced method to fabricate surface-disordered Zn_2SnO_4/SnO_2 hybrid nanocomposites, which exhibited improved sun-light driven degradation performance of organic pollutant owing to the introduction of oxygen vacancy and amorphous shells. However, the promotion of light absorption capacity is limited only by the introduction of defects. It is desirable to indraught narrowed band photocatalyst for further boosting of the light adsorption of the Zn_2SnO_4/SnO_2 hybrid. Ho et al. [15] prepared a novel visible-light-response photocatalyst $Zn_2SnO_4-SnO_2$/graphene (rGO) with improved photo-reactivity, and the results showed that rGO performed as an electron mediator to favor the high photocatalytic efficiency toward acetone and NO oxidation. Despite the previous achievements mentioned above, it is still a challenge to achieve a novel, multi-component $Zn_2SnO_4-SnO_2$-based photocatalyst by simultaneously extending the light absorption range and increasing the spatial separation of photogenerated charge carriers.

Cu_2O is regarded as a promising candidate for visible-light photocatalyst owing to its suitable band-gap (2.1–2.4 eV), amazing optical property, low cost, non-toxicity, and environmental acceptability [18–21]. However, pure Cu_2O has a short charge diffusion length (20–100 nm), resulting in a high recombination rate of photoinduced electron-hole pairs and quite low quantum efficiency [22]. For this purpose, as an efficient co-catalyst, Cu_2O could be added into some photocatalyst systems, e.g., ZnO [21,23], TiO_2 [24,25], CdS [26], $ZnWO_4$ [27], WO_3 [19,28], $BiVO_4$ [29], BiOBr [30], in order to broaden light absorption scope, facilitate charge carriers transfer and separation, and then boost up the photocatalytic performance. Inspired by previously reported achievements, we developed a novel "directing growth-etching treatment-coupling composites" route to prepare $Zn_2SnO_4/SnO_2/Cu_2O$ hybrid photocatalyst based on structural modulation and band alignment modification in this work. After the overall modification mentioned above, the as-obtained $Zn_2SnO_4/SnO_2/Cu_2O$ hybrids were simultaneously endowed with a higher specific surface area, wider spectral absorption range, and more efficient spatial separation of photogenerated charge carriers, giving rise to an enormous improvement of photodegradation efficiency for the removal of RhB. To our certain knowledge, this is the first report on the fabrication and insight into the mechanism of enhanced photocatalytic behavior of $Zn_2SnO_4/SnO_2/Cu_2O$ hybrids.

2. Materials and Methods

2.1. Materials

Sodium stannate tetrahydrate ($Na_2SnO_3 \cdot 4H_2O$), zinc acetate dehydrate ($Zn(CH_3COO)_2 \cdot 2H_2O$), EDTA disodium (EDTA-2Na), sodium hydroxide (NaOH), lysine, copper nitrate penthydrate ($Cu(NO_3)_2 \cdot 5H_2O$), ascorbic acid (AA), and rhodamine B (RhB) were all obtained from Sinopharm Chemical Reagent CO., Ltd. (Shanghai, China). Ethanol and ethylenediamine (EDA) were purchased from Fuyu Fine Chemical Reagent CO., Ltd. (Tianjin, China). All the chemicals used in this work were of analytical grade without further purification.

2.2. Synthesis of Pristine Zn_2SnO_4/SnO_2 Hierarchical Architectures (P-ZSO/SnO_2)

P-ZSO/SnO$_2$ was fabricated through a facile solvothermal synthesis procedure. Briefly, 1 mmol of $Zn(CH_3COO)_2 \cdot 2H_2O$ and 2.5 mmol of $Na_2SnO_3 \cdot 4H_2O$ were respectively put into the mixed solvents containing 27 mL deionized water, 8 mL EDA and 5 mL anhydrous alcohol under intense stirring to form a transparent solution. For simplicity, the solution containing Zn^{2+} was denoted as solution A, while the solution containing Sn^{4+} as solution B. The solution A was slowly dripped into solution B under vigorous stirring. After that, 0.2 mmol of lysine was added to the above mixture, which was continuously kept stirring for another 30 min. The obtained suspension was transferred into a 100 mL Teflon-lined autoclave, and maintained at 190 °C for 20 h. After being naturally cooled to room temperature (the cooling time is about 7 h), the white precipitate was centrifuged and washed with deionized water and anhydrous alcohol repeatedly. The resulting precipitate was dried at 70 °C in an electric drying oven overnight, and then grinded into powder. The as-obtained product was named P-ZSO/SnO$_2$. For comparison, Zn_2SnO_4/SnO_2 microspheres (M-ZSO) were prepared via a facile route, and the detailed procedure was presented in the supporting information.

2.3. Synthesis of Etching Zn_2SnO_4/SnO_2 Hierarchical Architectures (ET-ZSO/SnO_2)

First, 0.5 g of P-ZSO/SnO$_2$ was added to a 60 mL sodium hydroxide (5 M) solution with constant stirring for 20 min. Then, the suspension mentioned above was transferred into a 100 mL Teflon-lined autoclave and kept at 60 °C for 1 h. The subsequent washing and drying process was similar to that of P-Zn$_2$SnO$_4$/SnO$_2$. The as-obtained product was denoted as ET-ZSO/SnO$_2$.

2.4. Synthesis of $Zn_2SnO_4/SnO_2/Cu_2O$ Hierarchical Architectures

Typically, 0.02 mmol EDTA-2Na, 0.02 mmol $Cu(NO_3)_2 \cdot 5H_2O$ and a specified amount of ET-ZSO/SnO$_2$ were put into 50 mL deionized water to form a suspension, and sonicated for 30 min. 0.05 mmol NaOH and 0.1 mmol AA were respectively dissolved into 20 mL deionized water under constant stirring. The NaOH-solution was added dropwise into the suspension, and then followed by the sluggish drip of the AA-solution with vigorous stirring for another 40 min. The above mixture was stirred for 240 min at room temperature. The resulting product was treated by centrifuging and washing with deionized (D.I.) water and anhydrous alcohol to eliminate the impurity, followed by drying at 120 °C in a vacuum oven overnight. In this manner, coupling composites of 0.5, 1, 1.5, and 2% Cu$_2$O loaded onto ET-ZSO/SnO$_2$ were prepared and denoted as ZSC0.5, ZSC1, ZSC1.5 and ZSC2, respectively.

2.5. Characterizations

The crystal structure analysis of P-ZSO/SnO$_2$, ET-ZSO/SnO$_2$, and ZSC hybrids were performed by using a D8 Advance X–ray diffractometer (Bruker, Billerica, MA, USA) with a copper radiation ($\lambda = 0.15406$ nm). An ESCALAB 250Xi spectrometer (Thermo Fisher Scientific, New York, NY, USA)

equipped with a monochromatic Al-Kα radiation was employed to examine the surface component of P-ZSO/SnO$_2$ and ZSC hybrids. Morphological and micro-structural investigations of P-ZSO/SnO$_2$ and ZSC hybrids were achieved on a Hitachi-S-4800 field emission scanning electron microscope (Hitachi, Toyko, Japan) as well as JEM-2100F transmission electron microscope (JEOL Ltd., Tokyo, Japan). The Brunauer–Emmett–Teller (BET) specific surface area of P-ZSO/SnO$_2$ and ZSC hybrids was determined on the basis of multi-point estimation using a NOVA-2000e sorption analyzer. UV-DRS of P-ZSO/SnO$_2$, ET-ZSO/SnO$_2$ and ZSC hybrids were collected on a TU 1901 UV–vis spectrophotometer (Puxi, Beijing, China), using BaSO$_4$ as a reference. Photoluminescence (PL) spectra excited with a wavelength of 320 nm were achieved on a LS55 fluorescence spectrophotometer (PE, Waltham, MA, USA).

2.6. Photocatalytic Experiments

Commonly used RhB dye in the textile industry was taken as a model pollutant in our work. The procedure of RhB photodegradation tests were performed in a homemade apparatus, which was reported in our previous studies [10–12,31,32]. Briefly, 50 mg of photocatalyst was coated on the bottom surface of the culture dish (9 cm) to form a thin film, followed by dispersing into 40 mL RhB aqueous solution (1.0×10^{-5} M). Two daylight lamps (60 W, $\lambda \geq 420$ nm) were designated as the visible light source for triggering the photodegration reaction of RhB. After a specified interval of the simulant sun-light illumination, the suspension was sampled and the concentration of the reacted RhB aqueous solution was measured on a TU 1901 UV–vis spectrophotometer with the wavelength ranging from 300 nm to 700 nm.

2.7. Photocurrent Measurements

The photo-electrochemical measurements of P-ZSO/SnO$_2$, Cu$_2$O, and ZSC1.5 samples were carried out on a three-electrode CHI660E electrochemical workstation (Chenhua Instruments Co., Shanghai, China), which contained the counter electrode (Pt wire), reference electrode (saturated Ag/AgCl), and working electrode (photocatalysts). The details for the photo-electrochemical measurements were presented in our previously reported study [31,32].

3. Results and Discussion

Considering that 3D hierarchical architectures composed of one dimensional (1D) nanobuilding blocks, with desired size, shape and composition, play substantial roles in determining the photo-activity of photocatalysts, the morphological structure and composition of the as-obtained products were characterized by field emission scanning electron microscope (FESEM) in combination with EDS analysis, and TEM. From the FESEM image with low-magnification (Figure 1a), P-ZSO/SnO$_2$ was made up of massive flower-like architectures. High-magnification FESEM micrograph (Figure 1b) revealed clearly morphological structure that 3D flower-like architectures of P-ZSO/SnO$_2$ were comprised of a large number of closely interconnected 1D nanorod building blocks with small size. Comparing Figure 1b with Figure 1c, we can easily find that the ZSC1.5 sample almost inherited the hierarchical morphology of the corresponding P-ZSO/SnO$_2$ product, signifying that the etching process in combination with chemical deposition procedure used in this experiment only exerted a limited effect on the morphological structure. Such a special morphological structure will be beneficial for achieving high photo-activity [33–35]. The result of energy dispersive spectrometer (EDS) mapping (Figure 1e) perfectly authenticated the coexistence and homogeneous distribution of Zn, Sn, O, and Cu elements throughout the ZSC1.5 sample. Additionally, as is seen from Supplementary Figure S1, the M-ZSO sample was composed of microsphere-shaped particles with the size ranging from 1 to 2 µm.

A deep insight into detailed structural features of the ZSC1.5 sample was provided by TEM observation, as shown in Figure 2a,b. Obviously, the obtained ZSC1.5 sample exhibited 3D flower-like architectures with a mean size of 100–200 nm, built up from plenty of nanorods with an average diameter of approximately 10–20 nm. A close-view of a single unit was revealed from Figure 2b that oriented nanorods (referring to ZSO and SnO_2) were grown together with the common part in the middle and congregated with each other to shape into flower-like architectures. Noticeably, fine discrete Cu_2O nanoparticles were tightly anchored on the surface of ZSO and SnO_2 nanorods to establish an intimate contact along the interface between ZSO, SnO_2 and Cu_2O, which would effectively accelerate the interfacial charge migration and separation.
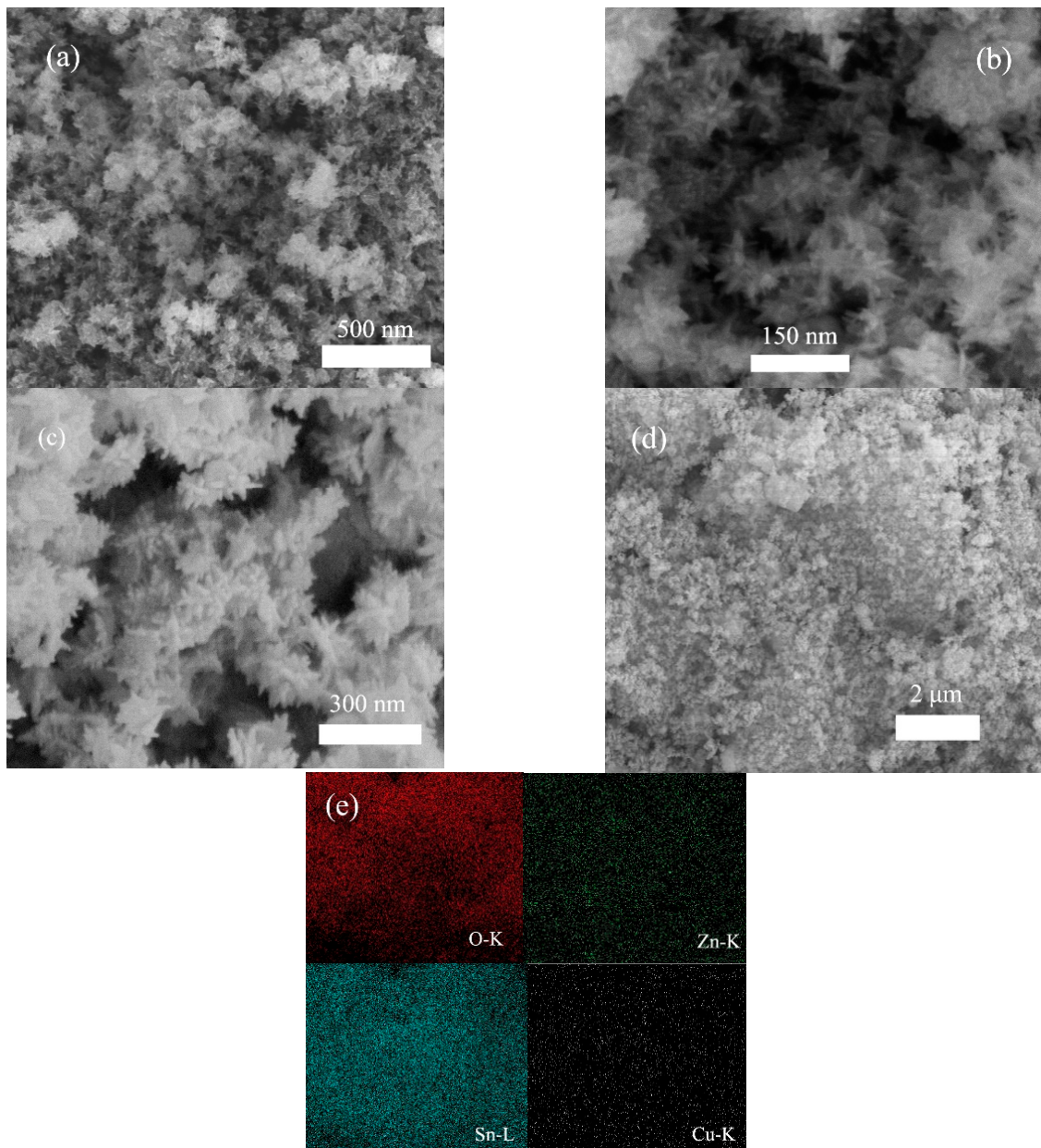

Figure 1. (**a**,**b**) Low-magnification and high-magnification FESEM images of P-ZSO/SnO_2, (**c**) FESEM image of the ZSC1.5 sample, (**d**,**e**) SEM image and its corresponding EDS mapping of the ZSC1.5 sample.
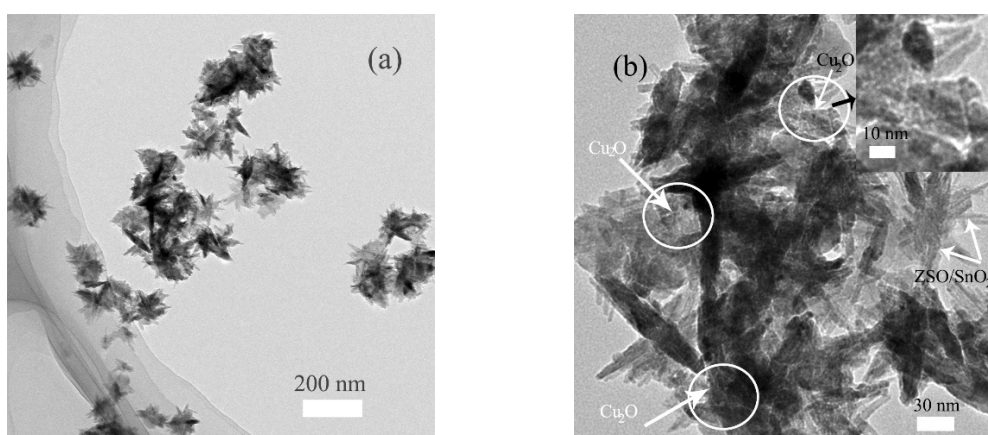
Figure 2. (**a**) Low-magnification TEM image, and (**b**) high-magnification TEM image as well as partially magnified image in the inset of the ZSC1.5 sample.

Figure 3 depicts the XRD patterns of P-ZSO/SnO$_2$, ET-ZSO/SnO$_2$, ZSC1.5, and Cu$_2$O samples. Clearly, only two crystalline phases of ZSO and SnO$_2$ can be perfectly identified in P-ZSO/SnO$_2$, well indexed to JCPDS card no. 74-2184 and 41-1445, respectively. No other diffraction peaks resulting from other residues or impurity phases, e.g., ZnO, were found, indicating the successful synthesis of the as-obtained product. Notably, the ET-ZSO/SnO$_2$ sample also had the same crystalline phases with P-ZSO/SnO$_2$ even through the etching process, although the corresponding diffraction peaks became broader and the diffraction peak intensity of ET-ZSO/SnO$_2$ grew weaker, compared with those of P-ZSO/SnO$_2$. Other than ZSO and SnO$_2$, no crystal phase related with Cu$_2$O was detected in the ZSC1.5 sample, which might be attributed to the low concentration of Cu$_2$O in comparison with that of ZSO and SnO$_2$. On the other hand, pure Cu$_2$O has sharp diffraction peaks, which are well indexed to JCPDS card no. 05-0667. Based on the analysis of XRD results, the possible etching mechanism for ZSO and SnO$_2$ could be proposed as following. Being subject to a high concentrated solution of NaOH, Zn^{2+} and Sn^{4+} could respectively coordinate with a specified amount of OH$^-$ to form soluble complex radicals of Zn(OH)$_4^{2-}$ and Sn(OH)$_6^{2-}$ under hydrothermal condition. As a result, the components of ZSO and SnO$_2$ were continuously converted into soluble complex radicals and dissolved into the solution with hydrothermal time prolonging. In fact, the mass of P-ZSO/SnO$_2$ decreased to a certain degree after etching treatment. Thus, such an explanation can be completely supported by the result that there is little difference in crystal phase and morphological structure before and after the etching treatment.
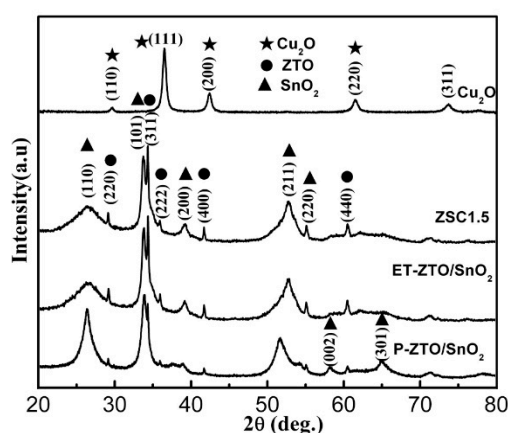

Figure 3. XRD patterns of P-ZSO/SnO$_2$, ET-ZSO/SnO$_2$, ZSC1.5, and Cu$_2$O samples.

　　　XPS analysis was taken to further inspect the surface component and valence status of the ZSC1.5 sample. The full scale XPS spectrum (Figure 4a) is constituted with four elements of O, Zn, Sn, and Cu, which is in good agreement with the result of EDS mapping. Referring to previously reported work, the asymmetric spectrum of O 1s (Figure 4b) can be divided into three peaks with binding energies at 530.5, 531.5 and 532.6 eV, which can be respectively denoted as lattice oxygen, vacancy oxygen, and chemisorbed oxygen species [17,36,37]. The vacancy oxygen species play a crucial effect on the visible-light photo-activity, as they are capable of inducing the formation of shallow energy levels. In terms of Zn 2p spectrum (Figure 4c), two fitting peaks with bind energies at ~1044.6 and 1022.4 eV could be ascribed to Zn 2p1$_{/2}$ and Zn 2p3$_{/2}$, respectively [15,17]. The prominent peaks centred at ~495.2 and 486.8 eV in Figure 4d can be assigned to the Sn 3d$_{1/2}$ and Sn 3d $_{3/2}$ of Sn^{4+} valence state. As for the chemical status of Cu element, the high-resolution spectrum of Cu 2p displayed two characteristic peaks with binding energies at ~952.4 and 932.7 eV, which verified the existence of Cu$_2$O in the ZSC1.5 sample. Moreover, by calculation, the concentration of Cu$_2$O is 1.4 wt%, being approximate to the theoretical value.
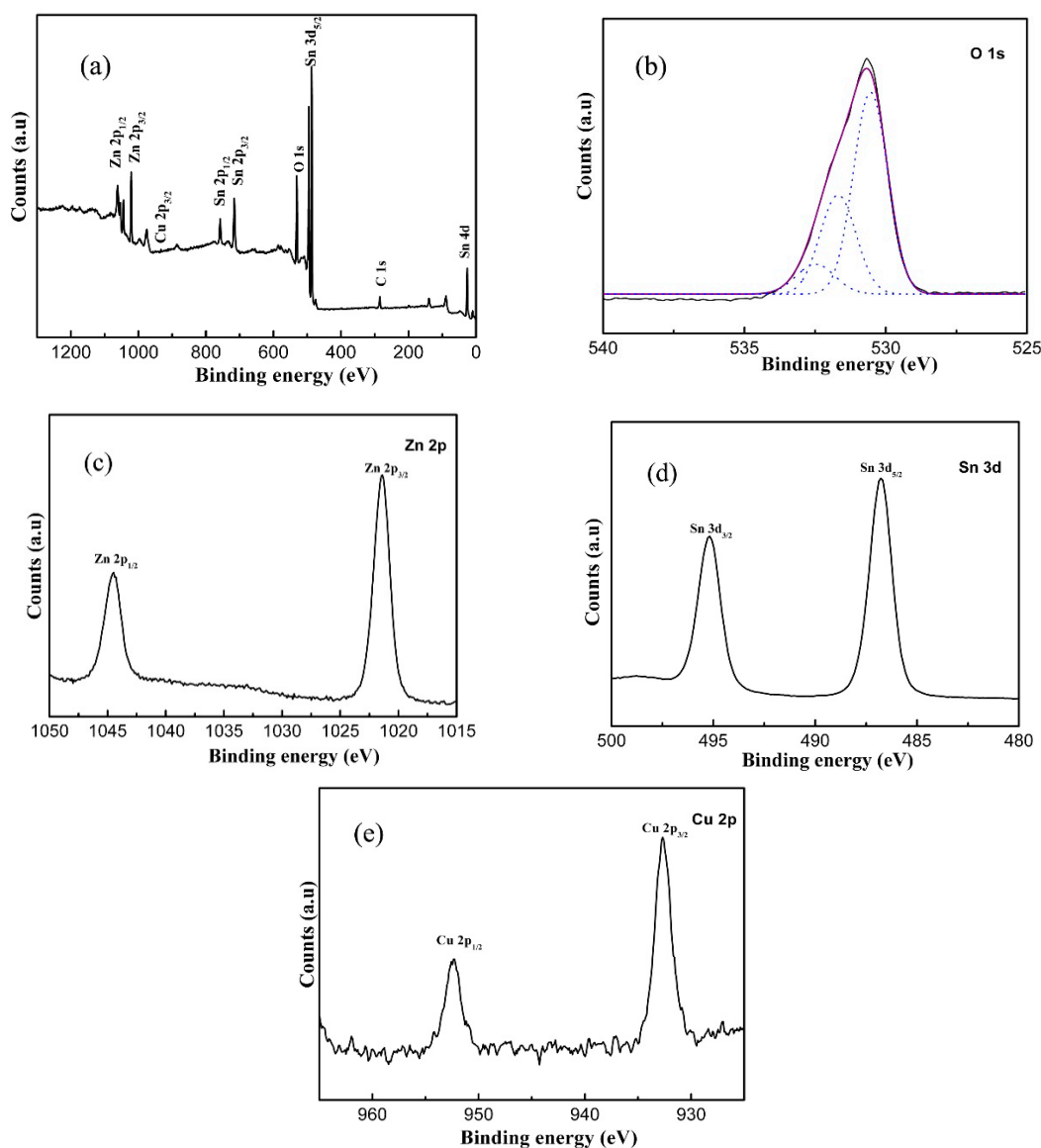

Figure 4. XPS spectra of the ZSC1.5 sample: (**a**) survey spectrum, (**b**) O 1s, (**c**) Zn 2p, (**d**) Sn 3d, (**e**) Cu 2p.

It is common knowledge that photocatalytic redox reactions occur on the interface between photocatalysts and pollutants. As one of the most significant factors affecting the photo-activity of photocatalysts, absorption capacity is highly dependent on the surface specific area. Generally speaking, a photocatalyst with a larger surface area is likely to adsorb more pollutant molecules, being indicative of its excellent absorption capacity. As a consequence, the specific surface area, together with the porosity of the as-obtained products, was evaluated through nitrogen adsorption-desorption measurements. It is unambiguous from Figure 5a that three samples all displayed type IV isotherm accompanying with typical H3 hysteresis loop in the light of Brunauer-Deming-Deming-Teller (BDDT) classification, signifying the appearance of slit-like mesopores because of subunits stacking [16]. Consulting to the Brunauer–Emmett–Teller (BET) method, the specific surface area (S_{BET}) of P-ZSO/SnO$_2$, ET-ZSO/SnO$_2$ and ZSC1.5 samples were approximately calculated to be 22.4 m^2/g, 49.2 m^2/g and 43.5 m^2/g, respectively. By contrast, the S_{BET} value of ET-ZSO/SnO$_2$ was much larger than that of P-ZSO/SnO$_2$, signifying that the absorption capacity of ET-ZSO/SnO$_2$ would be substantially enhanced due to the introduction of etching treatment. Although a slight decrease in the S_{BET} value occurred after Cu$_2$O decoration, it is still rationally inferred that the ZSC1.5 sample will be provided with more active sites and exceptional absorption capacity as a novel photocatalyst, as compared with P-ZSO/SnO$_2$. From Figure 5b, it is easily found out that all three samples contained mesopores ranging from 2nm to 50 nm. In comparison with P-ZSO/SnO$_2$, some more mesopores with small sizes appeared for ET-ZSO/SnO$_2$ and ZSC1.5, which was mainly attributed to the etching treatment and Cu$_2$O modification. Such special characteristics of surface area and porosity would promisingly lead to high photo-activity for a multi-component photocatalyst.
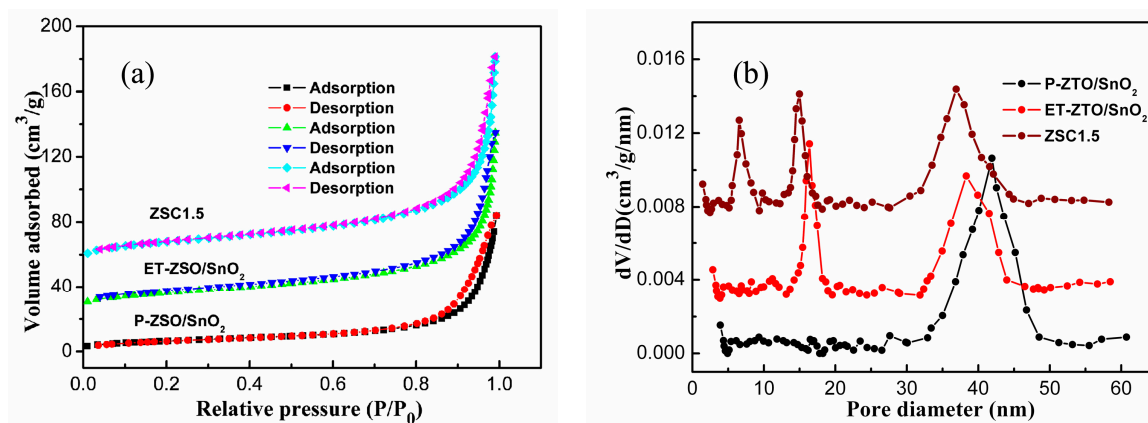

Figure 5. (**a**) The Nitrogen adsorption–desorption isotherm and (**b**) the corresponding pore size and distribution of P-ZSO/SnO$_2$, ET-ZSO/SnO$_2$ and ZSC1.5 samples.

In general, different kinds of photocatalysts exhibit different absorption features, either in the light absorption intensity or light absorption range. For this purpose, the diffuse reflection spectra (DRS) of pristine P-ZSO/SnO$_2$, ET-ZSO/SnO$_2$, and ZSC samples with different weight contents were taken and the results are given in Figure 6a. Either P-ZSO/SnO$_2$ or ET-ZSO/SnO$_2$ presented a reasonably poor visible-light absorption property due to the wide band-gap of ZSO and SnO$_2$. From another point of view, pure Cu$_2$O displayed a wide light response range and outstanding light harvesting in the whole visible light region. After ET-ZSO/SnO$_2$ are composited with Cu$_2$O, all ZSC samples expectedly displayed evidently enhanced optical absorption in the whole visible light region, imputing to the interaction between fine Cu$_2$O nanoparticles and ZSO and SnO$_2$ nanorod assemblies.
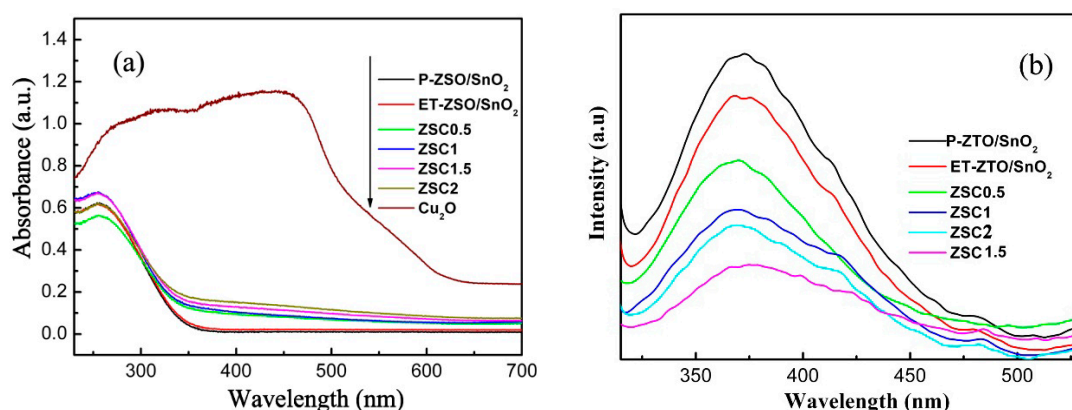
Figure 6. (**a**) UV–vis absorbance spectra of P-ZSO/SnO$_2$, ET-ZSO/SnO$_2$, and ZSC hybrids with different weight ratios, (**b**) PL spectra of P-ZSO/SnO$_2$, ET-ZSO/SnO$_2$, and ZSC hybrids with different weight ratios.

As is well known, photoluminescence (PL) emission spectrum is confirmed to be feasible and effective for revealing the migration and recombination of photo-induced hole-electron pairs [6,38]. Specifically, a lower PL intensity signifies the lower recombination possibility of photogenerated hole-electron pairs. For this purpose, PL measurements for pristine P-ZSO/SnO$_2$, ET-ZSO/SnO$_2$, and ZSC hybrids were performed and the results are presented in Figure 6b. For P-ZSO/SnO$_2$, the strongest intensity of PL emission peak was clearly indicative of the occurrence of the highest recombination possibility of photo-induced hole-electron pairs. With the addition of Cu$_2$O, the PL emission peak intensity of ZSC hybrids declined sharply at first, then reached the lowest value, and tended to rise thereafter. ZSC1.5 exhibited the lowest PL emission intensity, revealing that it had the most efficient suppression of charge carrier recombination in this hybrid system. Moreover, it is worth noting that the emission peak with weaker intensity (centred at about ~480 nm) is probably ascribed to oxygen vacancies [39,40]. Based on the analysis above, wider photoresponse range and more efficient spatial separation of photogenerated charge carriers were simultaneously achieved for ZSC hybrids through the co-modification with etching treatment and Cu$_2$O nanoparticle decoration.

In our work, the photocatalytic behaviour against the as-prepared photocatalysts was assessed with RhB as a target pollutant owing to its universal use and good long-term stability. For comparison, the photocatalytic degradation curve over M-ZSO is presented in Figure S2. Undoubtedly, the M-ZSO sample showed a very poor photocatalytic activity. Thus, it is particularly desired to carry out an overall investigation in order to explore the effect of the structural modulation and decoration on the photo-activity. As portrayed in Figure 7a, a certain amount of RhB molecules was adsorbed on the surface of photocatalysts during the absorption–desorption equilibrium process prior to illumination. By contrast, the adsorbed amount of RhB molecules for ET-ZSO/SnO$_2$ and ZSC samples with different weight contents was larger than that for P-ZSO/SnO$_2$, suggesting that the absorption capacity was indeed improved by the introduction of etching treatment, which was well consistent with the result of BET analysis. Under visible-light illumination, the absorbance values decreased continuously for all test samples. Among them, P-ZSO/SnO$_2$ displayed the worst photodegradation efficiency, mainly owing to its characteristics of energy band and morphological structure. For ET-ZSO/SnO$_2$ and ZSC samples, an evident improvement in photodegradation rate can be found, demonstrating that structural modulation combined with modification actually exerted a continuously positive effect on the photocatalytic performance. Specifically, the photodegradation efficiency of ZSC hybrids increased first with the Cu$_2$O loading amount and reduced thereafter. The ZSC 1.5 sample exhibited the highest photodegradation rate, approaching 98% over a period of 50 min of visible-light illumination. Perhaps, excess Cu$_2$O nanoparticles were likely to aggregate with each other and shadow the surface of ZSO and SnO$_2$ from the incident visible-light photons, resulting in poor light exposure of ZSO and SnO$_2$ for photo-induced charge carrier production. In order to quantitatively examine the reaction dynamics, we presumed that the photocatalytic behaviour for RhB aqueous solution followed the first-order kinetic

model plotted by the equation of $-\ln(C/C_0) = kt$, in which k, C_0 and C, respectively, stand for reaction rate constant, initial concentration, and concentration at time t of RhB concentration. From Figure 7b, it is very clear that ZSC1.5 had the highest kinetic constant of approximately 0.07 min^{-1}, which was around 7 and 6 times higher than that of P-ZSO/SnO$_2$ and ET-ZSO/SnO$_2$. Considering that the usability and stability are also vital factors other than photocatalytic efficiency in the potentially practical application, ZSC1.5 was determined as the representative to recycle RhB degradation experiments for five runs, in which the photocatalyst was recovered by centrifugation, washing and drying at 65 °C for 10 h. The stability result for ZSC1.5 is given in Figure 7c. Only a slight decline was detectable in the photodegradation rate from the first to the fifth run, perhaps resulting from inevitable weight loss in the process of collecting and washing. The as-obtained results are indicative of high stability of ZSC hybrid photocatalyst.

According to previously reported studies [41,42], the photocurrent response of photocatalysts can accurately shed light on photo-induced electrons and holes transfer and spatial separation. As a consequence, the photocurrent measurements of P-ZSO/SnO$_2$, Cu$_2$O and ZSC1.5 were carried out to further witness the contribution of Cu$_2$O to the charge carrier spatial separation efficiency of ZSC hybrids. As shown in Figure 8a, ZSC1.5 presented the largest photocurrent among all the tested samples, suggesting that it owned the longest charge carrier lifespan and highest spatial separation efficiency. Furthermore, the capacity of interfacial charge separation was revealed by electrochemical impedance spectra (EIS) Nyquist plots of P-ZSO/SnO$_2$, Cu$_2$O and ZSC1.5 electrodes under visible-light illumination, as depicted in Figure 8b. Evidently, ZSC1.5 had a much smaller arc radius than P-ZSO/SnO$_2$ and Cu$_2$O, which was attributed to its smaller charge transfer resistance and faster interfacial transfer rate of photoinduced charge carriers [43–45].
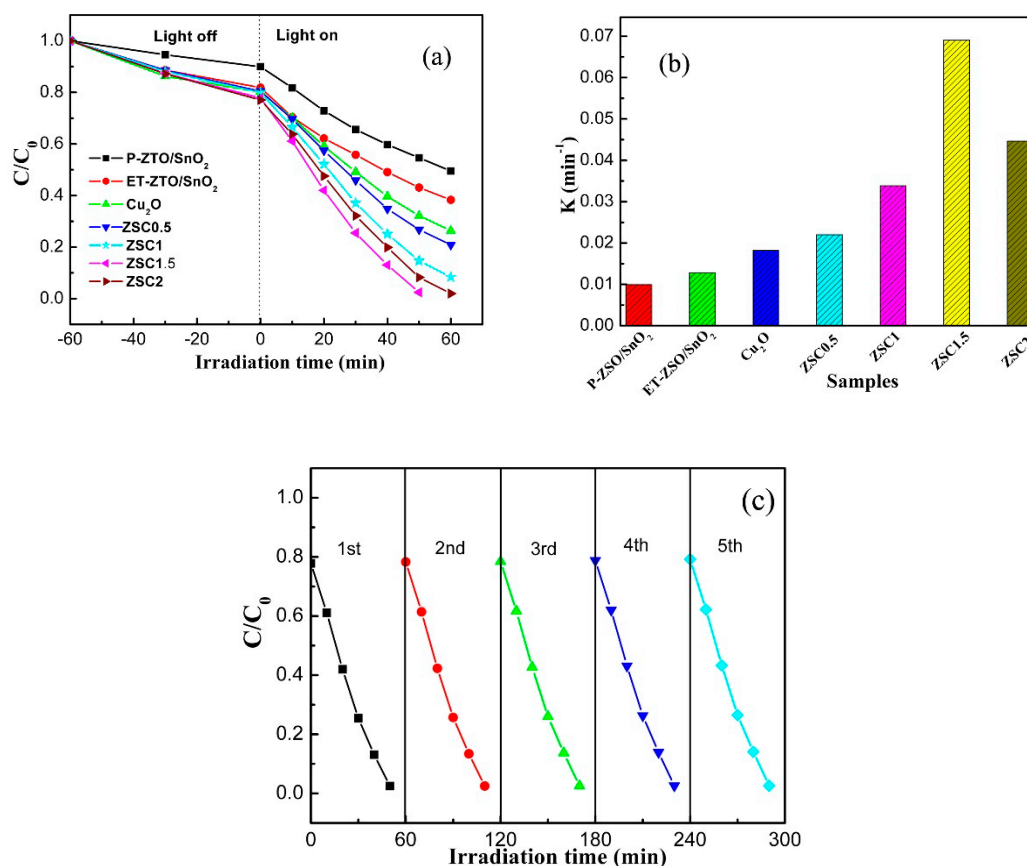

Figure 7. Photocatalytic degradation curves (**a**) and corresponding reaction kinetic constant curves (**b**) of P-ZSO/SnO$_2$, ET-ZSO/SnO$_2$, and ZSC hybrids with different weight ratios, (**c**) cycling runs in the photocatalytic degradation of RhB in the presence of ZSC1.5 sample.
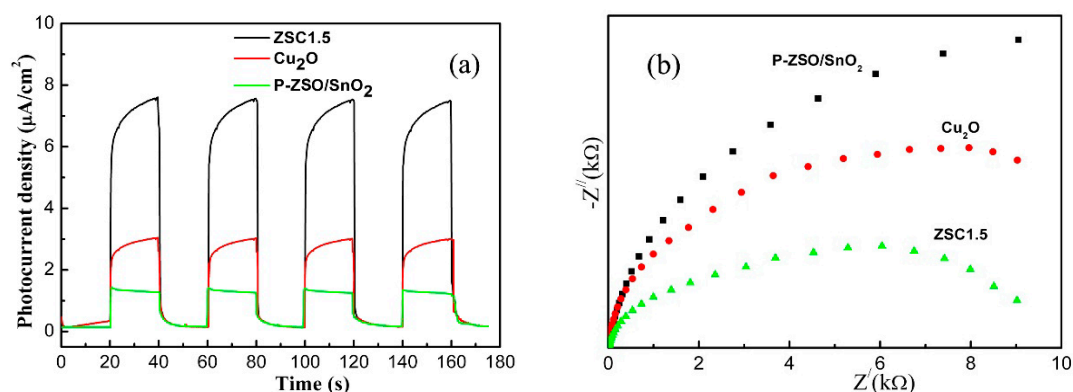
Figure 8. Transient photocurrents (**a**) and Electrochemical impedance spectra (**b**) of P-ZSO/SnO$_2$, Cu$_2$O, and ZSC hybrids electrodes under visible light irradiation (λ > 420 nm).

Trapping experiments were devised to reveal what active species would dominate the photodegradation reaction process in presence of ZSC1.5 photocatalyst. According to previous reports [46,47], four scavengers of benzoquinone (BZQ 2 mmol L^{-1}), sodium oxalate (SO, 4 mmol L^{-1}), tert-butyl-alcohol (t-BuOH, 2 mmol L^{-1}), and FeSO$_4$-EDTA (FS-EDTA, 0.2 mmol L^{-1}) were individually put into the system to capture the active species of $\bullet$O$_2^-$, h$^+$, $\bullet$OH and H$_2$O$_2$. The variation of photodegradation rate upon exposure to different scavengers is presented in Figure 9. Overall, the suppression effect on the photodegradation rate with the introduction of four scavengers followed the order of t-BuOH > BZQ > SO > FS-EDTA. Specifically, the photodegradation rate of RhB over ZSC 1.5 was only suppressed to some extent upon exposure to BZQ or t-BuOH, suggesting that the contribution of $\bullet$O$_2^-$ and $\bullet$OH was subordinate in the decomposition process. By contrast, the addition of SO and FS-EDTA led to an obviously significant decline in the photodegradation rate, implying that the active species of h$^+$ and H$_2$O$_2$ could make a predominant contribution to photocatalytic oxidation reaction of RhB.
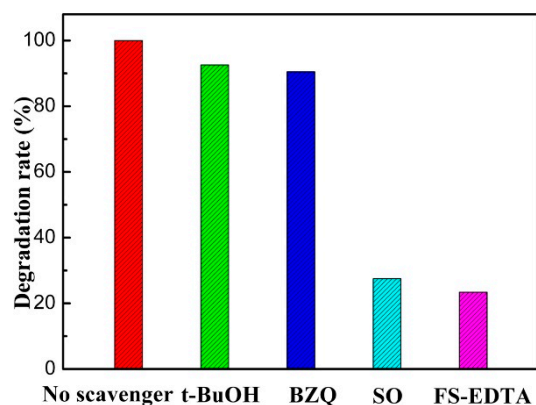

Figure 9. Effect of various scavengers on the visible-light photocatalytic performance of over the ZSC1.5 photocatalyst.

According to previous studies [15,21], the conduction band (CB) potentials for pure Cu$_2$O, Zn$_2$SnO$_4$, and SnO$_2$ are determined to be approximately -1.04 eV, -0.22 eV and 0.05 eV, respectively; while the valence band (VB) potentials for pure Cu$_2$O, Zn$_2$SnO$_4$, and SnO$_2$ are approximately 0.87 eV, 3.18 V and 3.25 eV, respectively. A proposed mechanism for the enormously promoted photocatalytic behavior is brought forth on the basis of energy-band structure combining with experimental results, as portrayed in Figure 10. In principle, pure Zn$_2$SnO$_4$ and SnO$_2$ belong to the group of wide bandgap semi-conducted photocatalysts, and are incapable of being excited to generate electron-hole pairs under visible-light irradiation. As is revealed by aforementioned results of XPS and PL measurements,

some defects, such as oxygen vacancy, existed in ZSC hybrid photocatalyst. As a result, shallow energy levels could be simultaneously produced in Zn_2SnO_4 and SnO_2 photocatalysts [14,15,48]. Upon exposure to visible light illumination, the electrons from show energy levels of Zn_2SnO_4 and SnO_2 are able to be excited and transfer to the CB positions of Zn_2SnO_4 and SnO_2, respectively. As for narrow-bandgap Cu_2O, the electrons from the VB position are easily excited, and then accumulate at the CB position through migration. Based on the energy band structure analysis above, a typical type II heterostructure is successfully established in the ternary component photocatalyst of Cu_2O, Zn_2SnO_4 and SnO_2. Assisted by the built-in electric field, the photoinduced electrons on the CB of Cu_2O could flow to that of Zn_2SnO_4, eventually arrive, and accumulate at the CB position of SnO_2. Simultaneously, the photoinduced holes from VB of SnO_2 are available to accumulate at the VB position of Cu_2O against the direction of the electron flow. Therefore, the efficient separation of photogenerated electron-hole pairs is successfully achieved in the ZSC hybrid system composed of Cu_2O, Zn_2SnO_4, and SnO_2 components with a well-matched band structure. It is worthwhile to note that the CB potential of SnO_2 (0.22 eV) is negative enough to enable electrons to react with O_2 and to generate the species of H_2O_2 (O_2/H_2O_2, 0.695 eV) [49–51], significantly playing a positive role in the photocatalytic oxidation process of RhB molecules. Although the VB potential of Cu_2O (0.87 eV) is not oxidative enough to convert the radicals of OH^- into the active species of OH ($OH^-/\bullet OH$, 1.99 eV) [52–55], the accumulated holes on the VB of Cu_2O could straightforwardly oxidize organic pollutant molecular to CO_2 and H_2O. That is why the active species of h^+ and H_2O_2 exerted a predominant contribution to the oxidization process of organic pollutant molecular.
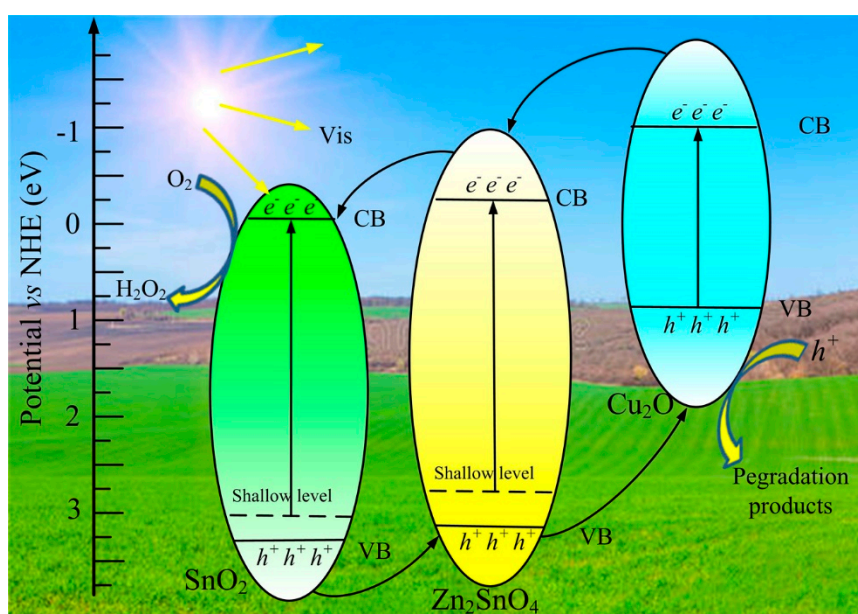

Figure 10. Schematic diagram of the charge transfer over the ZSC hybrids system under visible-light irradiation.

4. Conclusions

In summary, $Zn_2SnO_4/SnO_2/Cu_2O$ hybrid photocatalysts were successfully achieved via a novel "directing growth-etching treatment-coupling composites" route based on structural modulation and band alignment modification. The co-modification of the etching treatment and Cu_2O decoration endowed ZSC hybrid photocatalysts with a larger specific surface area, better light absorption ability, and more efficient spatial separation of photogenerated charge carriers. Thus, the resultant ZSC hybrid photocatalyst exhibited a continuously improved photocatalytic performance towards the photodegradation of RhB, as compared with the P-ZSO/SnO₂ sample. Especially, the k value of the ZSC1.5 photocatalyst reaches up to 0.07 min^{-1}, which was, respectively, about seven times higher than

the corresponding counterparts for the P-ZSO/SnO$_2$ sample. Such a simply and rationally designed route can provide an idea for the synthesis of highly efficient visible-light responsive photocatalysts applied in the territory of solar energy utilization and conversion.

Supplementary Materials: The following are available online at http://www.mdpi.com/2079-4991/9/10/1390/s1, Figure S1: SEM image of Zn$_2$SnO$_4$/SnO$_2$ microspheres, Figure S2: Photocatalytic degradation curve of Zn$_2$SnO$_4$/SnO$_2$ microspheres.

References

1. Tan, B.; Toman, E.; Li, Y.G.; Wu, Y.Y. Zinc stannate (Zn$_2$SnO$_4$) dye-sensitized solar cells. *J. Am. Chem. Soc.* **2007**, *129*, 4162–4163. [CrossRef] [PubMed]

2. Sumithra, S.; VictorJaya, N. Band gap tuning and room temperature ferromagnetism in Co doped Zinc stannate nanostructures. *Physica B* **2016**, *493*, 35–42. [CrossRef]

3. Lou, X.; Jia, X.; Xu, J.; Liu, S.; Cao, Q. Hydrothermal synthesis, characterization and photocatalytic properties of Zn$_2$SnO$_4$ nanocrystal. *Mater. Sci. Eng. A* **2006**, *432*, 221–225. [CrossRef]

4. Zhao, Q.Q.; Deng, X.L.; Ding, M.; Huang, J.Z.; Ju, D.X.; Xu, X.J. Synthesis of hollow cubic Zn$_2$SnO$_4$ sub-microstructures with enhanced photocatalytic performance. *J. Alloys Compd.* **2016**, *671*, 328–333. [CrossRef]

5. Li, Z.; Zhou, Y.; Zhang, J.; Tu, W.; Liu, Q.; Yu, T.; Zou, Z. Hexagonal nanoplate-textured micro-octahedron Zn$_2$SnO$_4$: Combined effects toward enhanced efficiencies of dye-sensitized solar cell and photoreduction of CO$_2$ into hydrocarbon fuels. *Cryst. Growth Des.* **2012**, *12*, 1476–1481. [CrossRef]

6. Liu, C.; Röder, R.; Zhang, L.; Ren, Z.; Chen, H.; Zhang, Z.; Ronning, C.; Gao, P.X. Highly efficient visible-light driven photocatalysts: A case of zinc stannate based nanocrystal assemblies. *J. Mater. Chem. A* **2014**, *2*, 4157–4167. [CrossRef]

7. Wang, J.; Li, H.; Meng, S.; Zhang, L.; Fu, X.; Chen, S. One-pot hydrothermal synthesis of highly efficient SnO$_x$-Zn$_2$SnO$_4$ composite photocatalyst for the degradation of methyl orange and gaseous benzene. *Appl. Catal. B Environ.* **2017**, *200*, 10–19. [CrossRef]

8. Junploy, P.; Phuruangrat, A.; Plubphon, N.; Thongtem, S.; Thongtem, T. Photocatalytic degradation of methylene blue by Zn$_2$SnO$_4$-SnO$_2$ system under UV visible radiation. *Mat. Sci. Semicon. Proc.* **2017**, *66*, 56–61. [CrossRef]

9. Jia, T.K.; Zhao, J.W.; Fu, F.; Deng, Z.; Wang, W.M.; Fu, Z.Y.; Meng, F.C. Synthesis, characterization and photcatalytic activity Zn-doped SnO$_2$/Zn$_2$SnO$_4$ coupled nanocomposites. *Int. J. Photoenergy* **2014**, *2014*, 7. [CrossRef]

10. Jia, T.K.; Fu, F.; Long, F.; Min, Z.Y.; Zhao, J.W.; Chen, J.; Li, J.L. Synthesis, characterization and enhanced visible-light photocatalytic activity of Zn$_2$SnO$_4$/C nanocomposites with truncated octahedron morphology. *Ceram. Int.* **2016**, *42*, 3808–3815. [CrossRef]

11. Jia, T.K.; Liu, M.; Yu, D.Y.; Long, F.; Mo, S.; Deng, Z.; Wang, W. A facile approach for the synthesis of Zn$_2$SnO$_4$/BiOBr nanocomposites with improved visible light photocatalytic performance. *Nanomaterials* **2018**, *8*, 313. [CrossRef] [PubMed]

12. Jia, T.K.; Fu, F.; Li, J.; Wang, W.; Hu, X. Constructing a novel Zn$_2$SnO$_4$/C/AgBr nanocomposite with extended spectral Response and improved photocatalytic performance. *J. Alloys Compd.* **2019**, *783*, 687–696. [CrossRef]

13. Sun, L.Q.; Han, X.; Jiang, Z.; Ye, Y.T.; Li, R.; Zhao, X.S.; Han, X.G. Fabrication of cubic Zn$_2$SnO$_4$/SnO$_2$ complex hollow structures and their sunlight-driven photocatalytic activity. *Nanoscale* **2016**, *8*, 12858–12862. [CrossRef] [PubMed]

14. Sun, S.Q.; Li, S.; Su, Y.; He, D.; Zhang, Z.T. Surface-disorder-engineered Zn_2SnO_4/SnO_2 hollow microboxes with enhanced solar-driven photocatalytic activity. *Appl. Surf. Sci.* **2019**, *463*, 474–480. [CrossRef]

15. Li, Y.; Wu, X.; Ho, W.; Lv, K.; Li, Q.; Li, M.; Lee, S.C. Graphene-induced formation of visible- light-responsive SnO_2-Zn_2SnO_4 Z scheme photocatalyst with surface vacancy for the enhanced photoreactivity towards NO and acetone oxidation. *Chem. Eng. J.* **2018**, *336*, 200–210. [CrossRef]

16. Ma, T.Y.; Cao, J.L.; Jaronies, M.; Qiao, S.Z. Interacting carbon nitride and titanium carbide nanosheets for high-performance oxygen evolution. *Angew. Chem. Int. Edit.* **2016**, *55*, 1138–1142. [CrossRef] [PubMed]

17. Zhou, X.; Li, X.; Sun, H.; Sun, P.; Liang, X.; Liu, F.; Hu, X.; Lu, G.Y. Enhanced gas sensing properties of monodisperse Zn_2SnO_4 octahedron functionalized by PdO nanoparticles. *Sensor. Actuat. B* **2018**, *266*, 302–310.

18. Paracchino, A.; Laporte, V.; Sivula, K.; Gratzel, M.; Thimsen, E. Highly active oxide photocathode for photoelectrochemical water reduction. *Nat. Mater.* **2011**, *10*, 456–461. [CrossRef]

19. Hu, C.C.; Nian, J.N.; Teng, H. Electrodeposited p-type Cu_2O as photocatalyst for H_2 evolution from water reduction in the presence of WO_3. *Sol. Energy Mater. Sol. Cells* **2008**, *92*, 1071–1076. [CrossRef]

20. Zhang, Z.; Wang, P. Highly stable copper oxide composite as an effective photocathode for water splitting via a facile electrochemical synthesis strategy. *J. Mater. Chem.* **2012**, *22*, 2456–2464. [CrossRef]

21. Siol, S.; Hellmann, J.C.; Tilley, D.S.; Graetzel, M.; Morasch, J.; Deuermeirer, J.; Jaegermann, W.; Klein, A. Band alignment engineering at Cu_2O/ZnO heterointerfaces. *ACS Appl. Mater. Interfaces* **2016**, *8*, 21824–21831. [CrossRef] [PubMed]

22. Jongh, P.E.; Vanmaekelbergh, D.; Kelly, J.J. Photoelectrochemistry of electrodeposited Cu_2O. *J. Electrochem. Soc.* **2000**, *147*, 486–489. [CrossRef]

23. Wang, Y.; Li, S.; Shi, H.; Yu, K. Facile synthesis of p-type Cu_2O/n-type ZnO nanoheterojunctions with novel photoluminescence properties enhanced field emission and photocatalytic activities. *Nanoscale* **2012**, *4*, 7817–7824. [CrossRef]

24. Yuan, W.; Yuan, J.; Xie, J.; Li, C.M. Polymer-mediated self-assembly of TiO_2@Cu_2O core-shell nanowire array for highly efficient photoelectrochemical water oxidation. *ACS Appl. Mater. Interfaces* **2016**, *8*, 6082–6092. [CrossRef] [PubMed]

25. Wang, M.Y.; Sun, L.; Lin, Z.Q.; Cai, J.H.; Xie, K.P.; Lin, C.J. P-N heterojunction photoelectrodes composed of Cu_2O-loaded TiO_2 nanotube arrays with enhanced photoelectrochemical and photoelectrocatalytic activities. *Energy Environ. Sci.* **2013**, *6*, 1211–1220. [CrossRef]

26. Cheng, W.Y.; Yu, T.H.; Chao, K.J.; Lu, S.Y. Cu_2O-decorated CdS nanostructures for high efficiency visible light driven hydrogen production. *Int. J. Hydrogen Energy* **2013**, *38*, 9665–9672. [CrossRef]

27. Tian, L.; Rui, Y.; Sun, K.; Cui, W.; An, W.J. Surface decoration of $ZnWO_4$ nanorods with Cu_2O nanoparticles to build heterostructure with enhanced photocatalysis. *Nanomaterials* **2018**, *8*, 33. [CrossRef]

28. Zhang, J.; Ma, H.; Liu, Z. Highly efficient photocatalyst based on all oxides WO_3/Cu_2O heterojunction for photoelectrochemical water splitting. *Appl. Catal. B* **2017**, *201*, 84–91. [CrossRef]

29. Wang, W.Z.; Huang, X.W.; Wu, S.; Zhou, Y.X.; Wang, L.J.; Shi, H.L.; Liang, Y.J.; Zou, B. Preparation of p-n junction Cu_2O/$BiVO_4$ heterogeneous nanostructures with enhanced visible-light photocatalytic activity. *Appl. Catal. B* **2013**, *134–135*, 293–301. [CrossRef]

30. Cui, W.; An, W.; Liu, L.; Hu, J.; Liang, Y. Novel Cu_2O quantum dots coupled flower-like BiOBr for enhanced photocatalytic degradation of organic contaminant. *J. Hazard. Mater.* **2014**, *280*, 417–427. [CrossRef]

31. Jia, T.K.; Fu, F.; Yu, D.; Cao, J.; Sun, G. Facile synthesis and characterization of N-doped TiO_2/C nanocomposites with enhanced visible-light photocatalytic performance. *Appl. Surf. Sci.* **2018**, *430*, 438–447. [CrossRef]

32. Jia, T.K.; Fu, F.; Li, J.L.; Deng, D.; Long, F.; Yu, D.; Cui, Q.; Wang, W.M. Rational construction of direct Z-scheme SnS-g-C_3N_4 hybrid photocatalyst for significant enhancement of visible-light photocatalytic activity. *Appl. Surf. Sci.* **2019**, *499*, 143941. [CrossRef]

33. Wang, W.; Zhu, H.G.; Li, B. Synergy of Ti-O-based heterojunction and hierarchical 1D nanobelt/3D microflower heteroarchitectures for enhanced photocatalytic tetracycline degradation and photoelectrochemical water splitting. *Chem. Eng. J.* **2019**, *378*, 122072. [CrossRef]

34. Jia, T.K.; Wang, W.M.; Long, F.; Fu, Z.Y.; Wang, H.; Zhang, Q.J. Synthesis, characterization, and photocatalytic activity of Zn-doped SnO_2 hierarchical architectures assembled by nanocones. *J. Phys. Chem. C* **2009**, *113*, 9071–9077. [CrossRef]

35. Lu, C.; Wang, J.; Xu, F.; Wang, A.Q.; Meng, D.W. Zn-doped SnO_2 hierarchical structures formed by a hydrothermal route with remarkably enhanced photocatalytic performance. *Ceram. Int.* **2018**, *44*, 15145–15152. [CrossRef]

36. Zhou, X.; Li, X.W.; Sun, H.B.; Sun, P.; Liang, X.S.; Liu, F.M.; Hu, X.L.; Lu, G.Y. Nanosheet-assembled $ZnFe_2O_4$ hollow microspheres for high-sensitive acetone sensor. *ACS Appl. Mater. Interfaces* **2015**, *7*, 15414–15421. [CrossRef] [PubMed]

37. Dupin, J.C.; Gonbeau, D.; Vinatier, P.; Levasseur, A. Systematic XPS studies of metal oxides, hydroxides and peroxides. *Phys. Chem. Chem. Phys.* **2000**, *2*, 1319–1324. [CrossRef]

38. Li, F.T.; Wang, Q.; Ran, J.R.; Hao, Y.J.; Wang, X.J.; Zhao, D.S.; Qiao, S.Z. Ionic liquid self-combustion synthesis of $BiOBr/Bi_{24}O_{31}Br_{10}$ heterojunctions with exceptional visible-light photocatalytic performances. *Nanoscale* **2015**, *7*, 1116–1126. [CrossRef]

39. Lin, H.F.; Liao, S.C.; Hung, W.W.; Hu, C.T. Thermal plasma synthesis and optical properties of Zn_2SnO_4 nanopowders. *Mater. Chem. Phys.* **2009**, *117*, 9–13. [CrossRef]

40. Pang, C.; Yan, B.; Liao, L.; Liu, B.; Zheng, Z.; Wu, T.; Yu, T. Synthesis characterization and opto-electrical properties of ternary Zn_2SnO_4 nanowires. *Nanotechnology* **2010**, *21*, 465706. [CrossRef]

41. Zhu, A.; Zhao, Q.; Li, X.; Shi, Y. $BiFeO_3/TiO_2$ nanotube arrays composite electrode: Construction characterization and enhanced photoelectrochemical properties. *ACS Appl. Mater. Interfaces* **2014**, *6*, 671–679. [CrossRef] [PubMed]

42. Huo, Y.; Yang, Y.; Dai, K.; Zhang, J.F. Construction of 2D/2D porous graphitic C_3N_4/SnS_2 composite as a direct Z-scheme system for efficient visible photocatalytic activity. *Appl. Surf. Sci.* **2019**, *481*, 1260–1269. [CrossRef]

43. Zhang, J.F.; Fu, J.W.; Wang, Z.L.; Cheng, B.; Dai, K.; Ho, W.K. Direct Z-scheme porous g-$C_3N_4/BiOI$ heterojunction for enhanced visible-light photocatalytic activity. *J. Alloys Compd.* **2018**, *766*, 841–850. [CrossRef]

44. Wang, Z.L.; Lv, J.L.; Zhang, J.F.; Dai, K.; Liang, C.H. Facile synthesis of Z-scheme $BiVO_4$/porous graphite carbon nitride heterojunction for enhanced visible-light-driven photocatalyst. *Appl. Surf. Sci.* **2018**, *430*, 595–602. [CrossRef]

45. Jiang, W.; Zong, X.; An, L.; Hua, S.; Miao, X.; Luan, S.; Wen, Y.; Tao, F.F.; Sun, Z. Consciously constructing heterojunction or direct Z-Scheme photocatalysts by regulating electron flow direction. *ACS Catal.* **2018**, *8*, 2209–2217. [CrossRef]

46. Zhu, B.; Xia, P.; Ho, W.; Yu, J. Isoelectric point and adsorption activity of porous g-C_3N_4. *Appl. Surf. Sci.* **2015**, *344*, 188–195. [CrossRef]

47. Li, S.T.; Shi, S.R.; Huang, G.C.; Xiong, Y.; Liu, S.W. Synergetic tuning charge dynamics and potentials of Ag_3PO_4 photocatalysts with boosting activity and stability by facile in-situ fluorination. *Appl. Surf. Sci.* **2018**, *455*, 1137–1149. [CrossRef]

48. Lee, J.; Kang, Y.; Hwang, C.S.; Han, S.; Lee, S.C.; Cho, J.H. Effect of oxygen vacancy on the structural and electronic characteristics of crystalline Zn_2SnO_4. *J. Mater. Chem. C* **2014**, *2*, 8381–8387. [CrossRef]

49. Dong, F.; Li, Q.; Sun, Y.; Ho, W.K. Noble metal-like behavior of plasmonic Bi particles as a cocatalyst deposited on $(BiO)_2CO_3$ microspheres for efficient visible light photocatalysis. *ACS Catal.* **2014**, *4*, 4341–4350. [CrossRef]

50. Di, J.; Xia, J.; Ji, M.; Wang, B.; Li, X.; Zhang, Q.; Chen, Z.; Li, H.M. Nitrogen-doped carbon quantum dots/BiOBr ultrathin nanosheets: In situ strong coupling and improved molecular oxygen activation ability under visible light irradiation. *ACS Sustain. Chem. Eng.* **2016**, *136*, 136–146. [CrossRef]

51. Shan, W.; Hu, Y.; Bai, Z.; Zheng, M.; Wei, C. In situ preparation of g-C_3N_4/bismuth-based oxide nanocomposites with enhanced photocatalytic activity. *Appl. Catal. B Environ.* **2016**, *188*, 12.

52. Kim, J.; Lee, C.W.; Choi, W. Platinized WO_3 as an environmental photocatalyst that generates OH radicals under visible light. *Environ. Sci. Technol.* **2010**, *44*, 6849–6854. [CrossRef] [PubMed]

53. Wang, X.; Li, S.; Yu, H.; Yu, J. In situ anion-exchange synthesis and photocatalytic activity of $Ag_8W_4O_{16}$/AgCl—nanoparticle core—shell nanorods. *J. Mol. Catal. A Chem.* **2011**, *334*, 52–59. [CrossRef]

54. Yu, H.; Liu, R.; Wang, X.; Wang, P.; Yu, J. Enhanced visible-light photocatalytic activity of Bi_2WO_6 nanoparticles by Ag_2O cocatalyst. *Appl. Catal. B Environ.* **2012**, *111–112*, 326–333. [CrossRef]

55. Li, Y.; Wang, J.; Yang, Y.; Zhang, Y.; He, D.; An, Q.; Cao, G.Z. Seed-induced growing various TiO$_2$ on nanostructures on g-C$_3$N$_4$ nanosheets with much enhanced photocatalytic activity under visible light. *J. Hazard. Mater.* **2015**, *292*, 79–89. [CrossRef] [PubMed]